Editors' Suggestion | Featured in Physics

Non-Abelian Electric Field and *Zitterbewegung* on a Photonic Frequency Chain

Shu Yang (杨树),[1,2] Bengy Tsz Tsun Wong (黄梓峻),[1,2] Jinbing Hu (胡金兵),[1,2,3] and Yi Yang (杨易)[1,2,*]

[1]*Department of Physics and HK Institute of Quantum Science and Technology, The University of Hong Kong, Pokfulam, Hong Kong, China*

[2]*State Key Laboratory of Optical Quantum Materials, The University of Hong Kong, Pokfulam, Hong Kong, China*

[3]*School of Optical-Electrical and Computer Engineering, University of Shanghai for Science and Technology, Shanghai 200093, China*

(Received 9 October 2025; revised 11 May 2026; accepted 15 May 2026; published 27 July 2026)

The synthetic frequency dimension, which realizes fictitious spatial dimensions from the spectral degree of freedom, has emerged as a promising platform for engineering artificial gauge fields in studying quantum simulations and topological physics with photons. A current central task for frequency-domain photons is the creation and manipulation of nontrivial non-Abelian field strength tensors and to observe their governing dynamics. Here, we experimentally demonstrate a minimal scheme for creating non-Abelian electric fields in a photonic frequency chain using a polarization-multiplexed, time-modulated ring resonator. By engineering spin-orbit coupling via modulation phase offset, polarization rotation, and polarization retardation, we achieve programmable control over synthetic Floquet bands and their quasimomentum spin-resolved textures. Leveraging self-heterodyne coherent detection, we demonstrate *Zitterbewegung*—a trembling motion of photons—induced by non-Abelian electric fields on the frequency chain. We further observe the interference between *Zitterbewegung* and Bloch oscillations arising from the coexistence of non-Abelian and Abelian electric fields. Our Letter bridges synthetic dimensions with non-Abelian gauge theory for versatile photonic emulation of relativistic quantum mechanics and spinor dynamics and can be instrumental in applications like frequency-domain optical computation and multimodal frequency comb control.

DOI: 10.1103/qy4y-171h

Synthetic non-Abelian gauge fields are fundamental building blocks for exploring topological physics and quantum dynamics in engineered physical platforms [1–7]. One crucial distinction between Abelian and non-Abelian gauge fields lies in their field strength. In Abelian electrodynamics governed by the U(1) gauge group, the field strengths solely depend on the spatial and temporal derivatives of the gauge fields, which preclude self-interaction [8]. Non-Abelian gauge theory generalizes this framework: electric fields and magnetic fields additionally depend on the noncommutativity between the matrix-valued scalar and vector potentials, enabling topological phenomena such as synthetic spin-orbit coupling (SOC) [9–21], nontrivial momentum spin texture [22–24], *Zitterbewegung* (ZB) dynamics [25–36], non-Abelian Hofstadter physics [37–39], and non-Abelian Aharonov-Bohm interference [40–50].

Photonic systems have recently emerged as an intriguing test bed for synthesizing non-Abelian fields. Among these, the synthetic frequency dimension [51–67] offers exceptional scalability, programmability, and compatibility with free-space, fiber, and integrated photonic architectures. Equipped with precise linear and nonlinear control, it holds promise for on-chip applications such as spectral shaping of light, frequency comb manipulation, and frequency-domain optical computation [68–74]. Polarization-multiplexed, time-modulated ring resonators are theoretically revealed to host frequency-domain non-Abelian fields across the Hermitian and non-Hermitian regimes [75–77] with a recent experimental demonstration of non-Abelian lattice gauge fields in a quasi-two-dimensional system under the twisted boundary condition [78]. Meanwhile, a recent theoretical study has extended SU(2) non-Abelian gauge fields to the SL(2, $\mathbb{C}$) gauge group based on the synthetic frequency dimension of an array of ring-resonator molecules [79]. However, existing research has primarily focused on non-Abelian magnetic fields for photons; the synthesis of their electric counterparts becomes crucial for the complete access and manipulation of the non-Abelian field strength tensor. Furthermore, fundamental phenomena like ZB dynamics induced by non-Abelian fields remain experimentally elusive in the photonic frequency dimension.

In this Letter, we experimentally realize a compact and versatile scheme for synthesizing non-Abelian electric fields on the photonic frequency chain based on a polarization-multiplexed, time-modulated ring resonator. We demonstrate the comprehensive control of the synthetic SOC via modulation phase offset, polarization rotation, and polarization retardation. Leveraging self-heterodyne

*Contact author: yiyg@hku.hk

 © 2026 American Physical Society

coherent detection, we further unveil ZB dynamics and their intricate interplay with Bloch oscillations (BOs), arising from the simultaneous presence of Abelian and non-Abelian electric fields.

The non-Abelian electric field is the 01-th component of the rank-two Yang-Mills field strength tensor,

$$E^i = -\partial A^i/\partial t - \nabla_i V - \mathrm{i}[V, A^i], \tag{1}$$

where all gauge field variables V and A^i are matrices and we assume a diag$(-+++)$ signature of the Minkowski metric. The time and spatial derivatives in Eq. (1) are inherited from the definition of the Abelian electric field, whereas the last term in Eq. (1) requires the noncommutativity between the scalar and vector potentials such that the non-Abelian part of the electric field can appear. To this end, we consider the lattice Hamiltonian [Fig. 1(a)]

$$\hat{H} = \sum_m \big[-\omega_y \hat{a}_m^\dagger \sigma_y \hat{a}_m - \omega_z \hat{a}_m^\dagger \sigma_z \hat{a}_m + J\hat{a}_m^\dagger \mathrm{e}^{-\mathrm{i}\theta\sigma_z}\hat{a}_{m+1} + J\hat{a}_{m+1}^\dagger \mathrm{e}^{\mathrm{i}\theta\sigma_z}\hat{a}_m\big], \tag{2}$$

where m indexes the lattice site, $\hat{a}_m^\dagger$ and $\hat{a}_m$ are the creation and annihilation operators, and $\sigma_{x,y,z}$ are Pauli matrices. Its corresponding Bloch Hamiltonian is

$$H(k) = 2J\cos(k + \theta\sigma_z) - \omega_y\sigma_y - \omega_z\sigma_z, \tag{3}$$

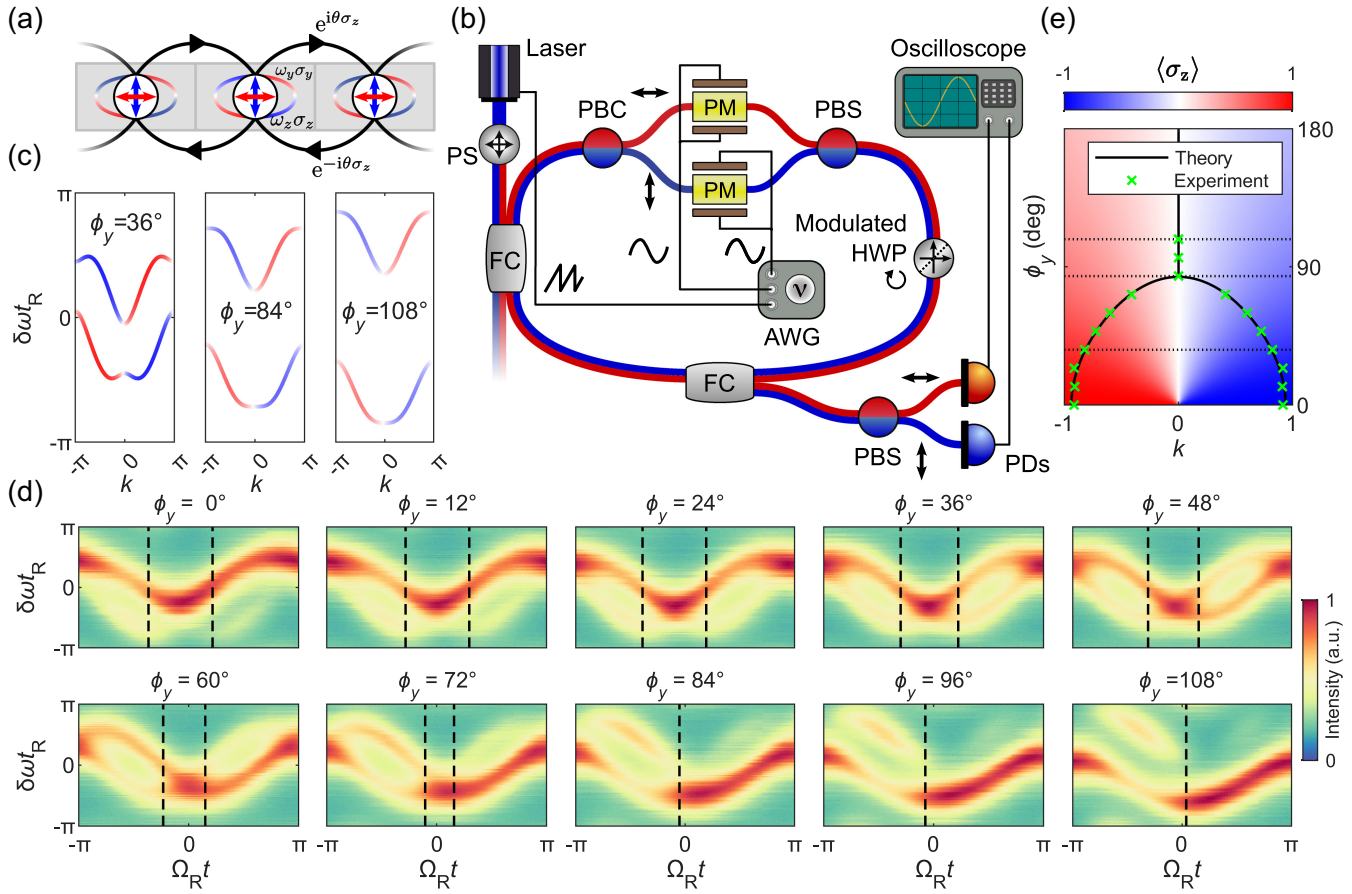

FIG. 1. Non-Abelian electric fields in the photonic frequency dimension. (a) One-dimensional lattice model featuring non-commutative matrix-valued scalar and vector potentials. (b) Simplified schematic of the experimental setup (see full setup in Supplemental Material Sec. S1 A [80]). The red and blue colors denote the horizontal and vertical polarization in the polarization-maintaining fibers, which are also labeled by the orientation of the double-sided arrows. Black lines correspond to electronic cables. PS, polarization synthesizer; FC, fiber coupler; PBS/C, polarization beam splitter and combiner; HWP, half-wave plate; PM, phase modulator; AWG, arbitrary waveform generator; PD, photodetector. (c) Band structure and spin texture of the theoretical model. The bands feature a double-minima to single-minima transition as the rotation ϕ_y increases. (d) Total intensity from both polarizations showing band structure evolution under ϕ_y sweeping. Dashed lines indicate the quasimomenta of the single-particle ground state. (e) Quasimomenta of the single-particle ground state overlaid with the heat map of the corresponding spin texture $\langle\sigma_z\rangle \equiv (I_\mathrm{h} - I_\mathrm{v})/(I_\mathrm{h} + I_\mathrm{v})$, where I_h and I_v are the intensity of the horizontal and vertical polarizations, respectively. The black solid line is the theoretical fitting for the experimental values (green crosses) obtained from (d). The three horizontal dotted cuts correspond to the band structures in (c). Here $\omega_z = 0$, $\theta = 0.31\pi$, $Jt_\mathrm{R} = -0.20\pi$.

which faithfully realizes a minimally coupled synthetic lattice under an equal mixing of Rashba and Dresselhaus SOC (see Supplemental Material Sec. S10 A [80]). The first two on-site terms in Eq. (2) contribute to a non-Abelian on-site scalar potential defined as $V = (-\omega_y\sigma_y - \omega_z\sigma_z)$, while the remaining hopping terms contain a non-Abelian vector potential $A_x = (-\theta\sigma_z)$. In this one-dimensional configuration, non-Abelian magnetic fields are absent for lack of flux; nevertheless, non-Abelian electric fields can still be defined as $\hat{E}_x = 2\omega_y\theta\sigma_x$ according to Eq. (1) due to the noncommutativity between the scalar and vector potentials, despite both being spatially homogeneous and temporally stationary.

To synthesize this Hamiltonian, we realize a polarization-multiplexed ring-resonator system as shown in Fig. 1(b), where we take the horizontal and vertical polarizations to represent the pseudo-spin-up and pseudo-spin-down states. This Hamiltonian is implemented by three controls: polarization-dependent phase modulation $g\cos(\Omega t \pm \theta)$ for the SU(2) hopping (where the modulation depth g relates to the hopping strength J by $J \approx -g/2t_R$ in the weak modulation limit $g \to 0$), polarization rotation for $\omega_y = \phi_y/t_R$, and differential phase retardation for $\omega_z = \phi_z/t_R$, where $t_R = 2\pi/\Omega_R$ is the round-trip time and Ω_R is the ring's free spectral range (FSR). The phase modulation frequency Ω is chosen near the Ω_R. Device-level implementation of the experiment is collected in the End Matter.

The SOC in the Hamiltonian leads to band gap opening and spin exchanges within the two bands as shown in Fig. 1(c). In the absence of ϕ_z, the lower band exhibits two energy-degenerate minima at $k = k_\pm$ for small ϕ_y. As ϕ_y increases, the two minima eventually merge at $k = 0$. Meanwhile, the spin texture also inverts upon traversing the avoided crossing of the two bands. We directly measure such band evolution in Figs. 1(d) and 1(e) by probing the light intensity from the dropping coupler while scanning the polarization rotation ϕ_y with a programmable polarization synthesizer serving as an electronically modulated half-wave plate. Figure 1(d) displays all ten frames of the measurements. For each measurement, we trace the energy bands and locate their ground-state quasimomenta $k \equiv \Omega_R t$ (see details in Supplemental Material Sec. S3 [80]), which are marked by one or two vertical dashed line(s) for each panel in Fig. 1(d). Such a collection of measured $k_\pm$ is plotted in Fig. 1(e) as green crosses, which can be well described by the theoretical expression of $k_\pm = \pm\sin^{-1}\sqrt{\sin^2\theta - \omega_y^2\cot^2\theta/4J^2}$ [77], where the parameters are fitted as $\theta = 0.3\pi$ and $Jt_R = -0.2\pi$ [solid line in Fig. 1(e)]. The fitted θ and J exhibit small offsets from their nominal values of $\theta = 0.25\pi$ and $Jt_R = -0.25\pi$, which likely results from the breakdown of the first-order approximation (see Supplemental Material Sec. S1 D [80]).

We demonstrate the spin texture exchanges of the two bands and the control of the single-particle ground state in Fig. 2, where we again perform the band spectroscopy but this time with ϕ_z turned on. The corresponding input-state preparation and calibration methods are summarized in the End Matter. In the experiment, two nonzero ϕ_z of opposite signs are chosen on the phase diagram [Fig. 2(a)], where the corresponding degeneracy-lifted new ground state is predicted to occur at positive and negative quasimomenta, respectively. Figure 2(b) shows the time-resolved intensity of the two polarizations and their contrast defined as $I_h - I_v$ for $\phi_z < 0$. Evidently, the two bands exchange their spin polarization, and the degeneracy of the ground state is lifted, with the ground-state quasimomentum being positive. Conversely, when a positive ϕ_z is chosen, the ground-state quasimomentum becomes negative, as observed in Fig. 2(c). In both Figs. 2(b) and 2(c), I_h exhibits a distinct linewidth and intensity reduction near the avoided crossing, and conversely for I_v. These features, absent in the low-loss limit, are consequences of loss-induced band broadening and can be modified upon the choice of the input state (see details in Supplemental Material Sec. S4 [80]). We have also performed analytical [Figs. 2(d) and 2(e)] and numerical [Figs. 2(f) and 2(g)] validation of the measurements [Figs. 2(b) and 2(c)]. The analytical model and computational simulation methods we adopt are summarized in the End Matter. Excellent agreement is achieved among the experimental data, the analytical calculations, and the numerical simulations as shown in Fig. 2.

A profound consequence of the synthesized non-Abelian electric fields is the emergence of ZB spectral dynamics, which manifests as an oscillatory motion of the center of mass (c.m.) of the spectral distribution of the optical field amplitude. This time-varying spectral distribution also repeats itself with a periodicity of Ω_R, reflecting the Floquet nature of the synthetic bands. Crucially, ZB differs from BO—another oscillatory dynamics but induced by Abelian electric fields [81]—in its modulation detuning dependence. While BO necessitates a nonzero frequency detuning to occur, ZB persists regardless of detuning, highlighting a fundamental distinction between the two dynamics in the frequency dimension (see Supplemental Material Sec. S11 [80]).

We are able to measure the ZB and BO phenomena and their interference in the spectral dynamics. Since this oscillation appears in the amplitude's frequency distribution, simple intensity detection in Fig. 1(b) is no longer sufficient. To directly resolve the electric field, we upgraded the detection scheme to a self-heterodyne coherent detection using balanced PD pairs. Additionally, the balanced PDs also eliminate the common-mode noise, hence improving the signal-to-noise ratio such that we can measure the weak ZB oscillations; see the End Matter for the interferometric implementation of the balanced detection.

Because the non-Abelian electric field is a function of ω_y, we can rapidly modulate $\phi_y = \omega_y t_R$ using the programmable synthesizer placed inside the ring and monitor

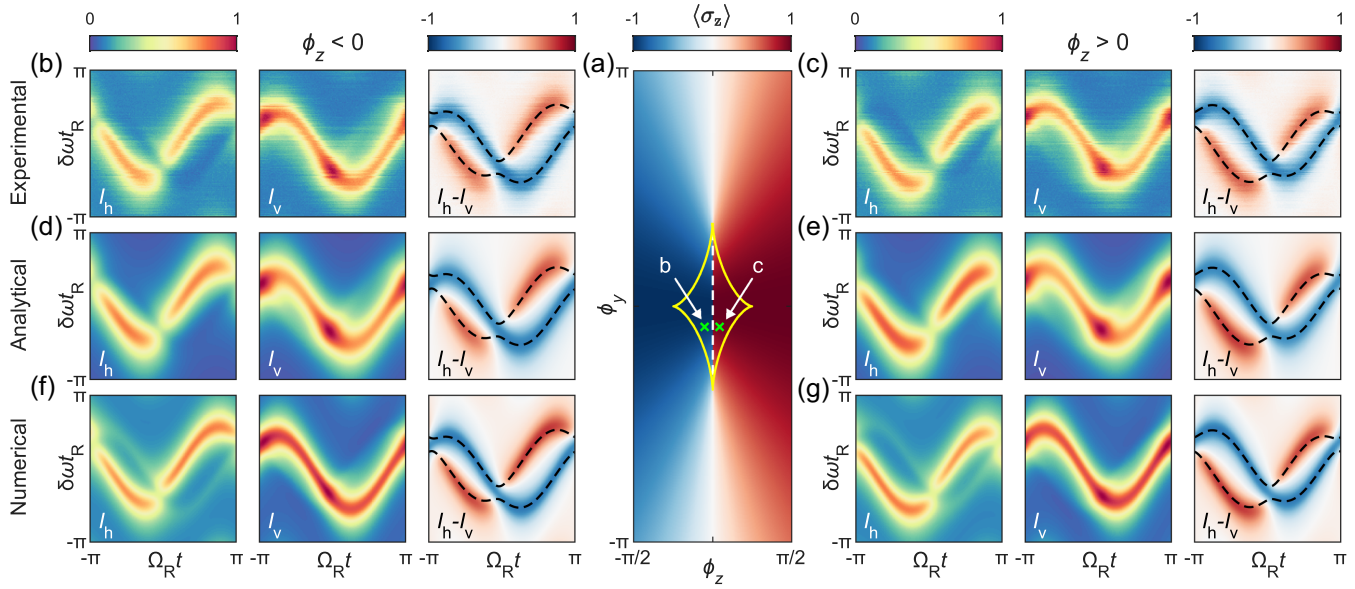

FIG. 2. Spin textures under synthetic spin-orbit coupling in the Floquet band structure. (a) Theoretical single-particle ground-state phase diagram overlaid with spin textures. Outside and inside the yellow solid curve, the SOC band possesses single and double local minima, while the white dashed line marks the ground-state degeneracy. The green crosses correspond to the measurements in (b) and (c). (b),(c) Experimentally measured, (d),(e) analytically calculated, and (f),(g) numerically simulated intensity spectra of the horizontal polarization (left), vertical polarization (middle), and their differences (right). The dashed curves depict the theoretical bands. A negative ϕ_z leads to a positive ground-state quasimomentum in (b), (d), and (f), whereas a positive ϕ_z leads to a negative ground-state quasimomentum in (c), (e), and (g). The experimental parameters, directly applied to the numerical simulations, are $\theta = 0.25\pi$, $\phi_y = -0.09\pi$, $g = 0.5\pi$, and $\gamma_R t_R = 0.63$, where the latter two are slightly modified as $g = 0.47\pi$ and $\gamma_R t_R = 0.83$ for the analytical calculation due to the violation of first-order approximations. $\phi_z = -0.05\pi$ for (b), (d), and (f), and $\phi_z = 0.04\pi$ for (c), (e), and (g).

the change of the center of mass $\Omega_{\text{c.m.}}$ induced by ZB along the frequency chain (see Supplemental Material Sec. S6 [80]). During the experiment, we swept the polarization rotation ϕ_y from 0 to 2π over four full cycles. We first measure the pure ZB phenomena in the absence of modulation frequency detuning $\Delta\Omega = 0$ and under weak modulation depth [Fig. 3(b)]. The oscillation frequency of the ZB dynamics is shown to be effectively tuned by the polarization rotation modulation and demonstrates clear 2π periodicity. The ZB oscillation frequency gets maximized at half of Ω_R when ϕ_y is near half-integers of 2π, whereas the ZB phenomenon vanishes for ϕ_y being integers of 2π.

Next, we demonstrate the interplay between BO and ZB in Fig. 3(c) by turning on the modulation frequency detuning $\Delta\Omega \equiv \Omega - \Omega_R$ while maintaining a weak modulation depth. The onset of $\Delta\Omega$ generates an Abelian electric field causing BO dynamics [81]. Therefore, under the coexisting Abelian and non-Abelian electric fields here, the measured spectral dynamics exhibits the simultaneous presence of a strong BO line at $\Omega_{\text{c.m.}} = \pm\Delta\Omega$ and the oscillatory ZB frequency trajectory. Moreover, both BO and ZB exhibit oscillations of their respective amplitudes that become most evident when the ZB frequency trajectory traverses the BO lines, indicating the strong interference between the two dynamics.

Finally, we enter the BO-dominant regime by further increasing the modulation depth [Fig. 3(d)]. While the BO frequency is solely determined by $\Delta\Omega$, its amplitude can be magnified by a stronger modulation depth. This becomes analytically transparent by defining a ratio between the BO and ZB intensity $\eta \equiv I_{\text{BO}}/I_{\text{ZB}} \sim |(2\omega_y/\Delta\Omega \sin\theta\cos k_0) + (8J^2 \sin\theta \sin^2 k_0/\omega_y \Delta\Omega \cos k_0)|^2$, where k_0 is the central momentum of the wave packet (details in Supplemental Material Sec. S11 [80]). Consequently, increasing $J \propto g$ renders BO progressively dominant over ZB, yet their interference remains evident. Moreover, the observed residual ZB features asymmetric amplitudes in the upper and lower halves of the ϕ_y modulation cycle, which may stem from the asymmetric phase response of the modulated synthesizer serving as the HWP inside the ring.

The measured complicated two-dynamics interference becomes analytically intractable, but we can still obtain numerical validations beyond the first-order approximations. The simulations are shown next to the experimental data in Figs. 3(b)–3(d), where major features agree well with the measurement. Moreover, the simulations further reveal intriguing fine features, in particular, the broadband interference fringes in Fig. 3(c), which are absent in the data due to noise and loss of coherence. Such fringes again arise from the interplay between BO and ZB: the detuned modulation causes BO, while also replicating ZB

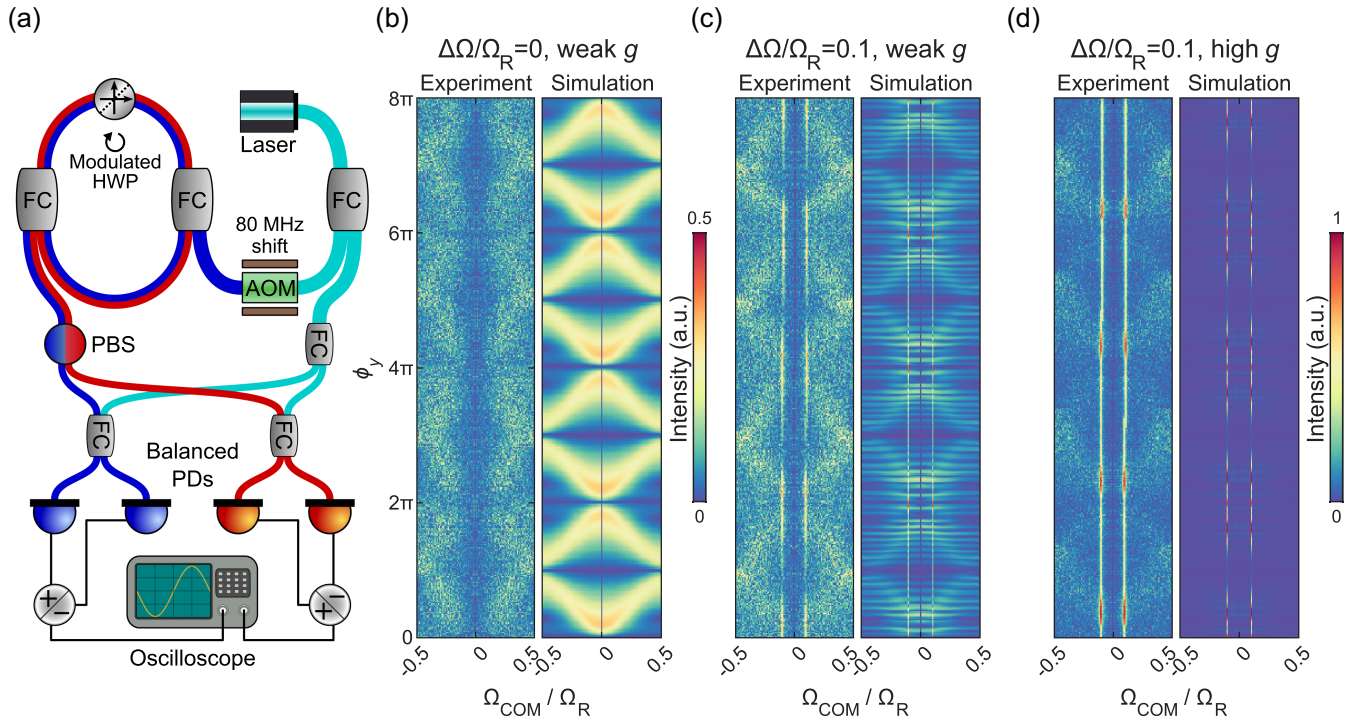

FIG. 3. Experimental signatures of *Zitterbewegung* spectral dynamics and its interplay with Bloch oscillations based on self-heterodyne coherent measurement. (a) Simplified schematic of the coherent detection setup. The rotation ϕ_y modulation is realized with the polarization synthesizer placed inside the ring, serving as a programmable HWP. Other optical elements inside the ring are omitted (see full setup in Supplemental Material Sec. S1 B [80]). The signals were shifted by 80 MHz using an acousto-optic modulator (AOM) before entering the ring. The output lights are sent to a pair of balanced PDs and interfere with the unshifted self-heterodyne reference light. (b) Pure ZB effect under a weak modulation depth and zero modulation detuning. (c) Simultaneous presence of ZB and BO and their interference under detuned weak modulation. (d) BO dominance under detuned strong modulation. All measurements are performed under input state $(0, 1)^{\mathrm{T}}$, retardation ϕ_z is calibrated near zero, and modulation phase offset $\theta = 0.25\pi$. In all spectra, the irrelevant spectral line corresponding to the base frequency component at $\Omega_{\mathrm{c.m.}} = 0$ is removed for better data presentation.

oscillations centered at the BO frequencies. The interference among different copies of ZB leads to the fringes in Fig. 3(c) (details in Supplemental Material Sec. S7 [80]).

The signal-to-noise ratio becomes limited in the time-resolved dynamics measurement, which hinders the quantitative comparison with simulations. In particular, the experimental spectra show an obscured region toward $\Omega_{\mathrm{c.m.}} = 0$ and miss the narrow theoretical gaps for ϕ_y at half-integers of 2π: both scenarios correspond to a weak designated polarization rotation. We therefore attribute these mainly to residual parasitic crosstalk between the two polarizations, which can exist even without the HWP due to finite extinction ratios of in-line components (around 18 dB for the fiber coupler and 22 dB for the PBS/C), imperfect connector alignment, and strain- and temperature-induced crosstalk in fiber components (see discussions of experimental limitations in Supplemental Material Sec. S1 D [80]).

Based on a polarization-multiplexed, time-modulated ring resonator, we experimentally synthesize non-Abelian electric fields and demonstrate their comprehensive control of spin-orbit coupling in the spin-resolved band structure measurements. Leveraging self-heterodyne detection, we observe the resulting dynamic phenomena of *Zitterbewegung* and its interference with Bloch oscillation under coexisting Abelian and non-Abelian electric fields.

The two-leg flux-ladder model [57] and its realization in the photonic frequency dimension [56], using clockwise-counterclockwise (CW-CCW) modes, can exhibit similar band structures as observed here. Nevertheless, U(1) Abelian fields appear in the natural orbital basis, and the SOC form manifests after a gauge transformation. Here, we use polarization as the pseudospin and implement matrix-valued gauge potentials via direct Peierls substitution, enabling the observation of ZB spectral dynamics. Moreover, the birefringent phase retardation between the two polarizations serves as an effective Zeeman coupling that lifts the ground-state degeneracy. Furthermore, the polarization and CW-CCW spinful degrees of freedom could be jointly utilized for a realization of SU(4) gauge fields (see Supplemental Material Sec. S12 [80]).

The demonstrated non-Abelian electric fields and spin-orbit coupling provide building blocks for explorations of non-Abelian topological physics with light [7] and

potential realizations of non-Abelian band topology [82] in synthetic frequency dimensions. The fiber-based experiment here can be further generalized to integrated platforms, in particular, thin-film lithium niobate, where transverse-electric and transverse-magnetic polarization coupling can be dispersion engineered [71]. By incorporating amplitude modulation, it is also possible to explore the non-Hermitian regime where non-Abelian fields can control complex-energy winding and braiding [76]. In the presence of nonlinearity, our setup could harbor soliton solutions to the mixed coupled nonlinear Schrödinger equations, and may further support frequency-domain dynamic gauge fields for photonic emulation of quantum chromodynamics based on photonic color degrees of freedom in the synthetic frequency dimension. Beyond the fundamental interest, the non-Abelian ZB-BO interference could offer a coherent knob to jointly steer the polarization texture and spectral distribution of polarization-multiplexed frequency combs, relevant for reconfigurable frequency-domain signal processing and transformations.

Acknowledgments—We thank Yu Xia, Chao Xiang, Xudong Zhang, and Xiaoqi Zhu for experimental support and Kun Ding and Zehai Pang for helpful discussions. J. H. acknowledges the support from the Natural Science Foundation of Shanghai (24ZR1453200) and White Magnolia Talent Program-Pujiang Project (25PJA106). The authors acknowledge the support from the National Natural Science Foundation of China Excellent Young Scientists Fund (12222417), the Hong Kong Research Grants Council through General Research Fund (17300525), Early Career Scheme (27300924), Strategic Topics Grant (STG3/E-704/23-N), Collaborative Research Fund (C7015-24GF and C7017-25E), Areas of Excellence Scheme (AoE/P-604/25-R), the Startup Fund of The University of Hong Kong, Ms. Belinda Hung, the Asian Young Scientist Fellowship, the Croucher Foundation, and the New Cornerstone Science Foundation through the Xplorer Prize.

Data availability—There are no publicly available research data or software supporting this manuscript. Requests for further information or data should be sent to the authors.

[1] J. Dalibard, F. Gerbier, G. Juzeliūnas, and P. Öhberg, Rev. Mod. Phys. **83**, 1523 (2011).
[2] N. Goldman, G. Juzeliūnas, P. Öhberg, and I. B. Spielman, Rep. Prog. Phys. **77**, 126401 (2014).
[3] M. Aidelsburger, S. Nascimbene, and N. Goldman, C. R. Phys. **19**, 394 (2018).
[4] T. Ozawa, H. M. Price, A. Amo, N. Goldman, M. Hafezi, L. Lu, M. C. Rechtsman, D. Schuster, J. Simon, O. Zilberberg *et al.*, Rev. Mod. Phys. **91**, 015006 (2019).
[5] M. C. Banuls, R. Blatt, J. Catani, A. Celi, J. I. Cirac, M. Dalmonte, L. Fallani, K. Jansen, M. Lewenstein, S. Montangero *et al.*, Eur. Phys. J. D **74**, 165 (2020).
[6] M. Aidelsburger, L. Barbiero, A. Bermudez, T. Chanda, A. Dauphin, D. González-Cuadra, P. R. Grzybowski, S. Hands, F. Jendrzejewski, J. Jünemann *et al.*, Phil. Trans. R. Soc. A **380**, 20210064 (2022).
[7] Y. Yang, B. Yang, G. Ma, J. Li, S. Zhang, and C. Chan, Science **383**, eadf9621 (2024).
[8] J. D. Jackson, *Classical Electrodynamics* (John Wiley & Sons, New York, 2012).
[9] J. Ruseckas, G. Juzeliūnas, P. Öhberg, and M. Fleischhauer, Phys. Rev. Lett. **95**, 010404 (2005).
[10] T. D. Stanescu, C. Zhang, and V. Galitski, Phys. Rev. Lett. **99**, 110403 (2007).
[11] Y.-J. Lin, K. Jiménez-García, and I. B. Spielman, Nature (London) **471**, 83 (2011).
[12] H. Zhai, Rep. Prog. Phys. **78**, 026001 (2015).
[13] S. Zhang, W. S. Cole, A. Paramekanti, and N. Trivedi, *Annual Review of Cold Atoms and Molecules* (World Scientific, 2015),pp. 135–179.
[14] L. Huang, Z. Meng, P. Wang, P. Peng, S.-L. Zhang, L. Chen, D. Li, Q. Zhou, and J. Zhang, Nat. Phys. **12**, 540 (2016).
[15] Z. Wu, L. Zhang, W. Sun, X.-T. Xu, B.-Z. Wang, S.-C. Ji, Y. Deng, S. Chen, X.-J. Liu, and J.-W. Pan, Science **354**, 83 (2016).
[16] K. Rechcińska, M. Król, R. Mazur, P. Morawiak, R. Mirek, K. Łempicka, W. Bardyszewski, M. Matuszewski, P. Kula, W. Piecek *et al.*, Science **366**, 727 (2019).
[17] V. G. Sala, D. D. Solnyshkov, I. Carusotto, T. Jacqmin, A. Lemaître, H. Terças, A. Nalitov, M. Abbarchi, E. Galopin, I. Sagnes, J. Bloch, G. Malpuech, and A. Amo, Phys. Rev. X **5**, 011034 (2015).
[18] J. Liang, W. Wen, F. Jin, Y. G. Rubo, T. C. Liew, and R. Su, Nat. Photonics **18**, 357 (2024).
[19] Y. Li, X. Ma, X. Zhai, M. Gao, H. Dai, S. Schumacher, and T. Gao, Nat. Commun. **13**, 3785 (2022).
[20] M. S. Spencer, Y. Fu, A. P. Schlaus, D. Hwang, Y. Dai, M. D. Smith, D. R. Gamelin, and X.-Y. Zhu, Sci. Adv. **7**, eabj7667 (2021).
[21] Y. Shi, Y. Gan, Y. Chen, Y. Wang, S. Ghosh, A. Kavokin, and Q. Xiong, Nat. Mater. **24**, 56 (2025).
[22] C. Whittaker, T. Dowling, A. Nalitov, A. Yulin, B. Royall, E. Clarke, M. Skolnick, I. Shelykh, and D. Krizhanovskii, Nat. Photonics **15**, 193 (2021).
[23] H. Terças, H. Flayac, D. D. Solnyshkov, and G. Malpuech, Phys. Rev. Lett. **112**, 066402 (2014).
[24] A. Gianfrate, O. Bleu, L. Dominici, V. Ardizzone, M. De Giorgi, D. Ballarini, G. Lerario, K. West, L. Pfeiffer, D. Solnyshkov *et al.*, Nature (London) **578**, 381 (2020).
[25] M. Merkl, F. Zimmer, G. Juzeliūnas, and P. Öhberg, Europhys. Lett. **83**, 54002 (2008).
[26] J. Y. Vaishnav and C. W. Clark, Phys. Rev. Lett. **100**, 153002 (2008).
[27] L. J. LeBlanc, M. Beeler, K. Jimenez-Garcia, A. R. Perry, S. Sugawa, R. Williams, and I. B. Spielman, New J. Phys. **15**, 073011 (2013).
[28] F. Dreisow, M. Heinrich, R. Keil, A. Tünnermann, S. Nolte, S. Longhi, and A. Szameit, Phys. Rev. Lett. **105**, 143902 (2010).

[29] C. Qu, C. Hamner, M. Gong, C. Zhang, and P. Engels, Phys. Rev. A **88**, 021604(R) (2013).
[30] X. Zhang, Phys. Rev. Lett. **100**, 113903 (2008).
[31] E. S. Sedov, Y. G. Rubo, and A. V. Kavokin, Phys. Rev. B **97**, 245312 (2018).
[32] M. Hasan, C. S. Madasu, K. D. Rathod, C. C. Kwong, C. Miniatura, F. Chevy, and D. Wilkowski, Phys. Rev. Lett. **129**, 130402 (2022).
[33] W. Zawadzki and T. M. Rusin, J. Phys. Condens. Matter **23**, 143201 (2011).
[34] L. Polimeno, A. Fieramosca, G. Lerario, L. De Marco, M. De Giorgi, D. Ballarini, L. Dominici, V. Ardizzone, M. Pugliese, C. Prontera *et al.*, Optica **8**, 1442 (2021).
[35] S. Lovett, P. M. Walker, A. Osipov, A. Yulin, P. U. Naik, C. E. Whittaker, I. A. Shelykh, M. S. Skolnick, and D. N. Krizhanovskii, Light Sci. Appl. **12**, 126 (2023).
[36] Y. Chen, R.-Y. Zhang, Z. Xiong, Z. H. Hang, J. Li, J. Q. Shen, and C. Chan, Nat. Commun. **10**, 3125 (2019).
[37] K. Osterloh, M. Baig, L. Santos, P. Zoller, and M. Lewenstein, Phys. Rev. Lett. **95**, 010403 (2005).
[38] N. Goldman, A. Kubasiak, A. Bermudez, P. Gaspard, M. Lewenstein, and M. A. Martin-Delgado, Phys. Rev. Lett. **103**, 035301 (2009).
[39] Y. Yang, B. Zhen, J. D. Joannopoulos, and M. Soljačić, Light Sci. Appl. **9**, 177 (2020).
[40] T. T. Wu and C. N. Yang, Phys. Rev. D **12**, 3845 (1975).
[41] F. Wilczek and A. Zee, Phys. Rev. Lett. **52**, 2111 (1984).
[42] P. A. Horváthy, Phys. Rev. D **33**, 407 (1986).
[43] A. Bohm, A. Mostafazadeh, H. Koizumi, Q. Niu, and J. Zwanziger, *The Geometric Phase in Quantum Systems: Foundations, Mathematical Concepts, and Applications in Molecular and Condensed Matter Physics* (Springer Science & Business Media, New York, 2013).
[44] Y. Yang, C. Peng, D. Zhu, H. Buljan, J. D. Joannopoulos, B. Zhen, and M. Soljačić, Science **365**, 1021 (2019).
[45] T. Iadecola, T. Schuster, and C. Chamon, Phys. Rev. Lett. **117**, 073901 (2016).
[46] J. Noh, T. Schuster, T. Iadecola, S. Huang, M. Wang, K. P. Chen, C. Chamon, and M. C. Rechtsman, Nat. Phys. **16**, 989 (2020).
[47] A. Jacob, P. Öhberg, G. Juzeliūnas, and L. Santos, Appl. Phys. B **89**, 439 (2007).
[48] Z. Dong, X. Wu, Y. Yang, P. Yu, X. Chen, and L. Yuan, Nat. Commun. **15**, 7392 (2024).
[49] M. Fruchart, Y. Zhou, and V. Vitelli, Nature (London) **577**, 636 (2020).
[50] J. Wu, Z. Wang, Y. Biao, F. Fei, S. Zhang, Z. Yin, Y. Hu, Z. Song, T. Wu, F. Song *et al.*, Natl. Electron. Rev. **5**, 635 (2022).
[51] L. Yuan, Q. Lin, M. Xiao, and S. Fan, Optica **5**, 1396 (2018).
[52] T. Ozawa, H. M. Price, N. Goldman, O. Zilberberg, and I. Carusotto, Phys. Rev. A **93**, 043827 (2016).
[53] B. A. Bell, K. Wang, A. S. Solntsev, D. N. Neshev, A. A. Sukhorukov, and B. J. Eggleton, Optica **4**, 1433 (2017).
[54] T. Ozawa and H. M. Price, Nat. Rev. Phys. **1**, 349 (2019).
[55] A. Dutt, M. Minkov, Q. Lin, L. Yuan, D. A. Miller, and S. Fan, Nat. Commun. **10**, 3122 (2019).
[56] A. Dutt, Q. Lin, L. Yuan, M. Minkov, M. Xiao, and S. Fan, Science **367**, 59 (2020).
[57] D. Hügel and B. Paredes, Phys. Rev. A **89**, 023619 (2014).
[58] S. Buddhiraju, A. Dutt, M. Minkov, I. A. Williamson, and S. Fan, Nat. Commun. **12**, 2401 (2021).
[59] E. Lustig and M. Segev, Adv. Opt. Photonics **13**, 426 (2021).
[60] N. Englebert, N. Goldman, M. Erkintalo, N. Mostaan, S.-P. Gorza, F. Leo, and J. Fatome, Nat. Phys. **19**, 1014 (2023).
[61] K. Wang, A. Dutt, K. Y. Yang, C. C. Wojcik, J. Vučković, and S. Fan, Science **371**, 1240 (2021).
[62] K. Wang, A. Dutt, C. C. Wojcik, and S. Fan, Nature (London) **598**, 59 (2021).
[63] H. Chen, N. Yang, C. Qin, W. Li, B. Wang, T. Han, C. Zhang, W. Liu, K. Wang, H. Long *et al.*, Light Sci. Appl. **10**, 48 (2021).
[64] A. Dutt, L. Yuan, K. Y. Yang, K. Wang, S. Buddhiraju, J. Vučković, and S. Fan, Nat. Commun. **13**, 3377 (2022).
[65] G. Villa, I. Carusotto, and T. Ozawa, Commun. Phys. **7**, 246 (2024).
[66] S. K. Sridhar, R. Srikanth, A. R. Miller, F. J. McComb, and A. Dutt, arXiv:2505.04151.
[67] D. Yu, W. Song, L. Wang, R. Srikanth, S. Kaushik Sridhar, T. Chen, C. Huang, G. Li, X. Qiao, X. Wu *et al.*, Photonics Insights **4**, R06 (2025).
[68] Y. Hu, C. Reimer, A. Shams-Ansari, M. Zhang, and M. Loncar, Optica **7**, 1189 (2020).
[69] H. Zhao, B. Li, H. Li, and M. Li, Nat. Commun. **13**, 5426 (2022).
[70] A. Balčytis, T. Ozawa, Y. Ota, S. Iwamoto, J. Maeda, and T. Baba, Sci. Adv. **8**, eabk0468 (2022).
[71] Y. Hu, M. Yu, N. Sinclair, D. Zhu, R. Cheng, C. Wang, and M. Lončar, Nat. Commun. **13**, 6293 (2022).
[72] H. X. Dinh, A. Balčytis, T. Ozawa, Y. Ota, G. Ren, T. Baba, S. Iwamoto, A. Mitchell, and T. G. Nguyen, Commun. Phys. **7**, 185 (2024).
[73] Z.-A. Wang, X.-D. Zeng, Y.-T. Wang, J.-M. Ren, C. Ao, Z.-P. Li, W. Liu, N.-J. Guo, L.-K. Xie, J.-Y. Liu *et al.*, Nat. Commun. **16**, 7780 (2025).
[74] X.-D. Zeng, Z.-A. Wang, J.-M. Ren, Y.-T. Wang, C. Ao, W. Liu, N.-J. Guo, L.-K. Xie, J.-Y. Liu, Y.-H. Ma, Y.-Q. Wu, S. Wang, P.-Y. Li, Z.-Q. Zhou, M. Yang, J.-S. Xu, X.-W. Luo, J.-S. Tang, C.-F. Li, and G.-C. Guo, arXiv:2508.15470.
[75] D. Cheng, K. Wang, and S. Fan, Phys. Rev. Lett. **130**, 083601 (2023).
[76] Z. Pang, B. T. T. Wong, J. Hu, and Y. Yang, Phys. Rev. Lett. **132**, 043804 (2024).
[77] B. T. T. Wong, S. Yang, Z. Pang, and Y. Yang, Phys. Rev. Lett. **134**, 163803 (2025).
[78] D. Cheng, K. Wang, C. Roques-Carmes, E. Lustig, O. Y. Long, H. Wang, and S. Fan, Nature (London) **637**, 52 (2025).
[79] Z. Dong, X. Chen, and L. Yuan, Nat. Commun. **16**, 10166 (2025).
[80] See Supplemental Material at http://link.aps.org/supplemental/10.1103/qy4y-171h for further discussions about the experimental results, along with details of experimental implementation, numerical simulation, and theoretical derivation, which includes Refs. [51,56,58,61,64,75,77].
[81] L. Yuan and S. Fan, Optica **3**, 1014 (2016).
[82] Q. Wu, A. A. Soluyanov, and T. Bzdušek, Science **365**, 1273 (2019).

End Matter

Experimental setup—Without loss of generality, we have assigned the horizontal and vertical polarizations as the pseudo-spin-up and pseudo-spin-down states, respectively. The main body of the ring resonator carries three major components: (i) A polarization-dependent cosinusoidal phase modulation with a modulation phase offset of $\pm\theta$ between the two polarization axes realizes the Peierls-substituted hopping in Eq. (3) containing the SU(2) vector potential. Its transfer function is $e^{ig\cos(\Omega t+\theta\sigma_z)}$, where the modulation frequency Ω is chosen near the ring's FSR Ω_R so that a one-dimensional spinful chain is formed by the polarization-multiplexed longitudinal modes of the ring. The modulation depth g relates to the hopping strength J by $J\approx -g/2t_R$ in the weak modulation limit $g\to 0$ and is implemented by two parallel lithium-niobate-based phase modulators between a pair of polarization beam splitters and combiners. (ii) A polarization rotation described by $e^{i\phi_y\sigma_y}$, where $\phi_y=\omega_y t_R$ enables coupling between the two polarizations and realizes the second term in Eq. (3). It is physically achieved by a tunable in-line HWP set at an angle of $\phi_y/2$. (iii) By applying different dc biases to the phase modulators, a phase retardation $e^{i\phi_z\sigma_z}$, where $\phi_z=\omega_z t_R$, can be introduced between the two polarizations to realize the third term in Eq. (3). The rotation (ii) and retardation (iii) jointly realize the SU(2) scalar potential.

Outside the ring, the arbitrary input state is prepared via a tunable continuous-wave laser followed by a polarization synthesizer, then injected into the ring resonator via a weakly coupled fiber coupler. Scanning across the synthetic dimension is achieved by applying a sawtooth signal to the tunable laser that produces a linear and periodic frequency detuning $\delta\omega$ over time. The synthesizer, when placed outside the ring, can deterministically prepare arbitrary polarization as the input state, while inside the ring, it can function as a programmable HWP to modulate the photon polarization rotation at a maximum rate of 100 kHz, which is crucial for the ZB dynamics and its ϕ_y dependence. The intracavity signals are sampled through another coupler and separated by a polarization beam splitter, after which each polarization intensity is obtained by a pair of photodetectors. The whole experiment is realized in an in-line polarization-maintaining manner, without utilizing single-mode fibers or free-space elements, to minimize uncontrollable polarization crosstalk and insertion loss. This approach eliminates the need for amplifiers inside the ring, thereby helping reduce the noise and enhance the coherence of the measurements.

Scanning of ϕ_y for band evolution—For the band evolution in Figs. 1(d) and 1(e), we do not require a specified input state for the optimal projection onto the eigenstates. Therefore, we put the synthesizer inside the ring, serving as an electronically modulated HWP to tune the polarization rotation ϕ_y at a repetition rate of 100 Hz for a 0°–108° scan by a step of 12°. The input laser frequency ω is detuned with a repetition rate of 1 kHz, so that a full FSR, and hence a full band, is scanned at every ϕ_y.

Spin texture exchange measurements—For the measurements in Fig. 2, the polarization rotation ϕ_y is fixed. We therefore replace the synthesizer with a mechanical in-line HWP and move the synthesizer outside the ring to prepare an input state that balances the projection of both polarizations. The retardation ϕ_z contains contributions from both the birefringence of the polarization-maintaining fibers and the dc biases applied to the phase modulators. The fiber's intrinsic birefringence can be large, but only its value modulo 2π is relevant and can be treated as constant during the measurement window since it is slow-varying. Hence, the total ϕ_z can be compensated and controlled by the phase modulators (see Supplemental Material Sec. S2 [80] for detailed ϕ_z calibration protocol).

Analytical and numerical modeling—Under the first-order approximation, the analytical intensity projections are given by $I_\alpha \propto \left|\sum_{j=1,2}\langle\psi_\alpha|\psi_j\rangle\langle\psi_j|\psi_{in}\rangle/\left(E_j-\delta\omega-i\gamma_R\right)\right|^2$, where $\alpha=\{h,v\}$, $|\psi_{1,2}\rangle$ are the eigenvectors of the Hamiltonian in Eq. (3), $|\psi_{in}\rangle$ is the input polarization state, $\delta\omega$ is the frequency detuning of the laser, and γ_R is the round-trip amplitude loss rate. $E_{1,2}$ are the k-dependent eigenenergies given by $E_\pm(k)=2J\cos\theta\cos k\pm\sqrt{\omega_y^2+\omega_z^2+4J^2\sin^2\theta\sin^2 k+4J\omega_z\sin\theta\sin k}$. On the other hand, we develop a time-domain signal processing toolbox that can comprehensively analyze both the system's steady-state and transient responses beyond the first-order approximation (see Supplemental Material Sec. S9 [80]). The method faithfully simulates the time-domain response via the transfer function $\mathbf{E}(t+t_R)=\mathbf{T}\cdot\mathbf{E}(t)$, where $\mathbf{E}=(E_h,E_v)^T$ is the photonic pseudospin and the transfer function $\mathbf{T}=e^{i\omega t_R-\gamma_R t_R}e^{ig\cos(\Omega t+\theta\sigma_z)}e^{i\phi_y\sigma_y}e^{i\phi_z\sigma_z}$.

Self-heterodyne dynamics measurement—As shown in Fig. 3(a), 1% of the source laser power is split off to serve as the self-heterodyne reference, with the remainder shifted by 80 MHz using an acousto-optic modulator before entering the ring. The two polarization components from the ring output are separated by a polarization beam splitter, and then each of them coherently interacts with the self-heterodyne reference in the 50:50 coupler and finally gets detected by a balanced photodetector pair (details in Supplemental Material Sec. S5 [80]).